Dynamic and Thermal Effects of the Tibetan and Iranian Plateaus on the Northward-Propagating Intraseasonal Oscillation during Boreal Summer

WENTING HU,[a,b] ANMIN DUAN,[c,a,b] BIAN HE,[a,b] AND SAI HAO[d]

[a] *State Key Laboratory of Numerical Modeling for Atmospheric Sciences and Geophysical Fluid Dynamics (LASG), Institute of Atmospheric Physics, Chinese Academy of Sciences, Beijing, China*
[b] *University of Chinese Academy of Sciences, Beijing, China*
[c] *State Key Laboratory of Marine Environmental Science, College of Ocean and Earth Sciences, Xiamen University, Xiamen, China*
[d] *National Marine Environmental Forecasting Center, Beijing, China*

(Manuscript received 14 April 2021, in final form 31 December 2021)

ABSTRACT: This study investigates the dynamic and thermal effects of the Tibetan and Iranian Plateaus (TIP) on the characteristics of the northward-propagating boreal summer intraseasonal oscillation (BSISO) and reveals associated physical mechanisms. The relative importance of the Tibetan Plateau (TP) and Iranian Plateau (IP) to the northward propagation of BSISO is also detected. The findings are based on comparative analyses of the control run and six sensitivity experiments using the atmospheric model component of CAS FGOALS-f3-L (the low-resolution version of the Chinese Academy of Sciences Flexible Global Ocean–Atmosphere–Land System model, finite-volume version 3). It is demonstrated that the absence of TIP surface sensible heat or terrain restricts the occurrence of upper-level easterly and lower-level westerly anomalies, as well as moisture convergence over the Asian summer monsoon (ASM) region, which leads to a weakened easterly vertical wind shear with a narrowed range and the generation of a negative meridional specific humidity gradient in the northern Bay of Bengal. These mean-state changes are not conducive to the formation of positive barotropic vorticity together with planetary boundary layer moisture convergence to the north of the convective center, thus impeding the northward propagation of the BSISO. Results indicate that the combined TIP area, via its dynamic and thermal effects, modulates the northward-propagating BSISO by directly affecting the vertical wind shear and meridional moisture gradient in the northern Indian Ocean. By contrast, the TP plays a decisive role in the BSISO northward propagation due to the limited dynamic and thermal effects of IP on the background circulation and water vapor convergence over the ASM region.

KEYWORDS: Forcing; Climate variability; Thermodynamics; Intraseasonal variability

1. Introduction

The Tibetan Plateau (TP), the largest highland region in the world, is located in the subtropics of the central-eastern Eurasian continent and has obvious impacts on the Asian climate (Tao and Ding 1981; Yanai et al. 1992; Zhao and Chen 2001; Duan and Wu 2005; Yasunari et al. 2006; Boos and Kuang 2010; Wu et al. 2015; He et al. 2019a; Liu et al. 2020). The dynamic blocking effect of the TP in boreal winter causes the westerly airflow to split into northern and southern branches and then merge on the leeward side of the plateau (Bolin 1950; Yeh 1950), which excites gravity waves and Rossby waves in the development of stationary waves (Held et al. 2002). During boreal summer, the TP, acting as a huge and elevated heat source (Flohn 1957; Yeh et al. 1957), plays critical roles in the generation, intensity, and variability of the Asian summer monsoon (ASM) (Ye and Wu 1998; Wu and Zhang 1998; Hsu and Liu 2003; Wu et al. 2012a; Duan et al. 2020).

To explain the thermal effects of the TP on summer monsoon rainfall, Wu et al. (1997, 2007) proposed that the surface sensible heat on the TP slope induces abundant moisture transport from the ocean to the land, subsequently leading to the generation of ASM precipitation, referred to as the sensible heat–driven air pump (SHAP). Such a thermally induced air pump also exists in the forcing of the Iranian Plateau (IP), another large-scale orography in the Eurasian continent (Wu et al. 2012b). The effects of sensible heat over the IP and TP on the climate of other regions can be mutually enhanced or offset (Liu et al. 2017). The combined pumping effect of the Tibetan and Iranian Plateaus (TIP) generates a TIP-SHAP that conveys moisture from the oceans and significantly influences the formation of the ASM (Wu et al. 2012b; Liu et al. 2020).

Previous studies showed that the ASM is not only modulated by the TIP/TP thermal conditions in the mean state or on the interannual to interdecadal time scales, but also critically influenced by the boreal summer intraseasonal oscillation (BSISO), which is characterized by significant northward propagation in the Indian sector and western North Pacific–East Asia (WNP-EA) region (e.g., Yasunari 1979; Krishnamurti and Subrahmanyam 1982; Wang and Rui 1990; Lee et al. 2013).

Denotes content that is immediately available upon publication as open access.

Supplemental information related to this paper is available at the Journals Online website: https://doi.org/10.1175/JCLI-D-21-0294.s1.

Corresponding author: Wenting Hu, hwt@lasg.iap.ac.cn

DOI: 10.1175/JCLI-D-21-0294.1

TABLE 1. Experiment design.

Name	Topography	Sensible heating	Description
AMIP-ctrl	Full	Full	AMIP experiment using the external forcings prescribed as their historical values. The model integration covered from 1970 to 2014. The daily outputs from 1997 to 2014 were provided for analysis.
AMIP-noTIPtopo	No TIP topography	Full	As in the AMIP-ctrl experiment, but the TIP topography above 500 m (red curve in Fig. 1a) was set to 500 m.
AMIP-noTIPsh	Full	No sensible heating over TIP	As in the AMIP-ctrl experiment, but the vertical diffusion heating term in the boundary layer scheme was set to zero within the TIP with elevations above 500 m. The TIP topography remained unchanged.
AMIP-noTPtopo	No TP topography	Full	As in the AMIP-ctrl experiment, but the TP topography above 500 m (blue curve in Fig. 1b) was removed.
AMIP-noTPsh	Full	No sensible heating over TP	As in the AMIP-ctrl experiment, but the surface sensible heating was not allowed to heat the atmosphere over TP where the topography was above 500 m. The TP topography remained unchanged.
AMIP-noIPtopo	No IP topography	Full	As in the AMIP-ctrl experiment, but the IP topography above 500 m (purple curve in Fig. 1c) was removed.
AMIP-noIPsh	Full	No sensible heating over IP	As in the AMIP-ctrl experiment, but the surface sensible heating was not allowed to heat the atmosphere over IP where the topography was above 500 m. The IP topography remained unchanged.

The northward propagation of the BSISO is known to be closely related to the active and break phases of the South Asian summer monsoon (Yasunari 1980; Krishnan et al. 2000; Ding and Wang 2009), the East Asian summer monsoon (Yang et al. 2010; Li et al. 2015; Wang et al. 2017; Zhu and Li 2017), tropical cyclone activities (Goswami et al. 2003; Kikuchi and Wang 2010; Moon et al. 2018), and extreme events (Hsu et al. 2016, 2017; Zhu and Li 2018).

Multiple mechanisms for the northward propagation of the BSISO have been proposed, mainly including surface hydrological effects (Webster 1983), Rossby wave emanation from the eastward-propagating convection near the equator (Wang and Xie 1997; Hsu et al. 2004), air–sea interactions (Kemball-Cook and Wang 2001; Fu et al. 2003; Fu and Wang 2004), easterly vertical zonal wind shear (Xie and Wang 1996; Jiang et al. 2004; Yang et al. 2019), planetary boundary layer (PBL) moisture advection (Jiang et al. 2004; DeMott et al. 2013), and cumulus momentum transport (Kang et al. 2010). DeMott et al. (2013) utilized both reanalysis and model data to emphasize that the vertical zonal wind shear and moisture advection in the PBL are the most dominant mechanisms responsible for the BSISO's northward propagation. In the presence of vertical wind shear, barotropic vorticity in the free atmosphere is generated, which further induces water vapor convergence in the PBL, leading to the northward movement of the convective center (Jiang et al. 2004). Moreover, PBL moisture advection, both via the mean flow and due to the mean meridional moisture gradient, contributes to the formation of moisture convergence, and thus convective heating, to the north of the convection center (Li and Wang 1994; Jiang et al. 2004; DeMott et al. 2013).

The northward-propagating BSISO influences the circulation, precipitation, and diabatic heating over the TP that show marked intraseasonal variations (Wang and Duan 2015; Hu et al. 2016; Zhong et al. 2020). However, how the dynamic and thermal effects of Asian large-scale orography affect the intensity and propagation of the BSISO has not received much attention, as previous studies have focused mainly on the climatic response in rainfall and circulation over the ASM region to altered TIP or TP terrain height and surface sensible heat in model simulations. Yang et al. (2019) examined the effects of lowered TP elevation on the northward-propagating BSISO. However, due to the dominance of TP thermal effects during boreal summer, it is also essential to explore the influences of changes in TIP thermal forcing on the characteristics and northward propagation of the BSISO. In addition, the relative importance of the TP and IP to the northward propagating BSISO needs further investigation. Therefore, the aims of this study are to explore the role of TIP orographic uplift and surface heat conditions in modulating the northward-propagating BSISO and examine which region is more important between TP and IP, and to reveal the underlying physical mechanisms.

The remainder of the paper is organized as follows: section 2 describes the data, methods, experiment design, and preliminary model evaluation. The differences among the changes in the characteristics of the BSISO with reduced orography or eliminated surface sensible heat over TIP, TP, and IP are analyzed in section 3. Section 4 explains the causes of the changes in the northward propagation of the BSISO under the dynamic and thermal forcing of Asian large-scale orography. And finally, conclusions and some further discussion are provided in section 5.

2. Data, experiment design, methods, and model evaluation

a. Observational datasets

The daily precipitation estimates of the Global Precipitation Climatology Project (GPCP), version 1.3 (Huffman et al. 2001), with a global 1° × 1° spatial resolution from 1997 to 2014, were used as the observed precipitation data (available from https://www.ncei.noaa.gov/data/global-precipitation-climatology-project-gpcp-daily/access/). Daily mean wind, air temperature, specific humidity, surface temperature, and surface pressure on a grid of 1.5° × 1.5° from the European Centre for Medium-Range Weather Forecasts (ECMWF) interim reanalysis (ERA-Interim) dataset (Dee et al. 2011) for the period 1997–2014 were utilized to detect the atmospheric horizontal circulation and vertical structure. The ERA-Interim dataset can be downloaded from http://apps.ecmwf.int/datasets/data/interim_full_daily.

b. Model and experiment design

The low-resolution version of the Chinese Academy of Sciences (CAS) Flexible Global Ocean–Atmosphere–Land System model, finite-volume version 3 (CAS FGOALS-f3-L) was utilized in this study, developed at the State Key Laboratory of Numerical Modeling for Atmospheric Sciences and Geophysical Fluid Dynamics (LASG), Institute of Atmospheric Physics (IAP), CAS. It consists of five components: atmosphere, ocean, land, and sea ice models and a coupled module. The atmospheric component is version 2.2 of the Finite-Volume Atmospheric Model (FAMIL) (Li et al. 2019), which has C96 horizontally and 32 layers vertically in hybrid coordinates. A detailed description of the model can be seen in He et al. (2019b, 2020).

To examine the dynamic and thermal effects of Asian large-scale orography on the northward propagation of intraseasonal oscillation during boreal summer, seven AMIP (Atmospheric Model Intercomparison Project) experiments were conducted as summarized in Table 1. The first experiment (AMIP-ctrl; http://doi.org/10.22033/ESGF/CMIP6.3182) served as the control run, while the other six sensitivity experiments modified the topography and surface sensible heating of the TIP, TP and IP based on the AMIP-ctrl test. For TIP region, the topography above 500 m (red curve in Fig. 1a) was set to 500 m in AMIP-noTIPtopo (http://doi.org/10.22033/ESGF/CMIP6.3186). In AMIP-noTIPsh (http://doi.org/10.22033/ESGF/CMIP6.3189), the vertical diffusion heating term in the boundary layer scheme was set to zero in the same region. In other words, the sensible heating was removed in the TIP where the topography was above 500 m but the TIP topography remained unchanged. The same modifications of topography and sensible heating for TIP were also applied to the TP (blue curve in Fig. 1b) and IP (purple curve in Fig. 1c) regions. As a result, four experiments were carried out, named herein AMIP-noTPtopo, AMIP-noTPsh, AMIP-noIPtopo, and AMIP-noIPsh. The model was integrated from 1970 to 2014, with the simulations for the last 18 years analyzed. The use of atmosphere-only model allows us to isolate internal atmospheric dynamics.

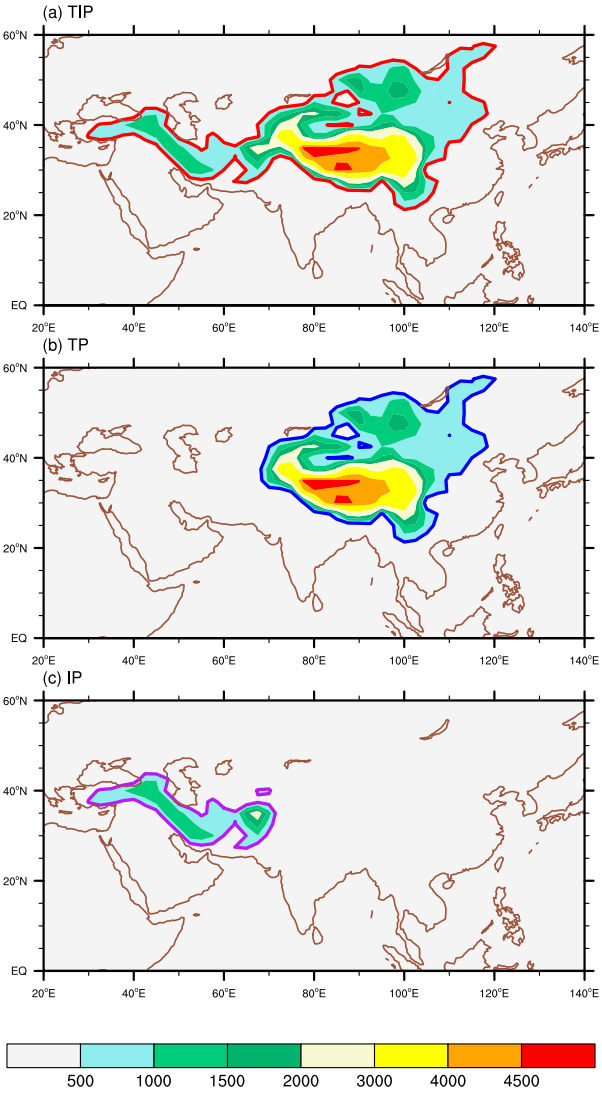

FIG. 1. Orographic regions specified for (a) the Tibetan and Iranian Plateaus (TIP) together, (b) the Tibetan Plateau (TP) only, and (c) the Iranian Plateau (IP) only. Red, blue, and purple contours denote the regions with an average altitude greater than 500 m of TIP, TP, and IP, respectively. The orographic data (shading; m) are derived from the AMIP-ctrl experiment of CAS FGOALS-f3-L.

c. Methods

All analyses in this study were based on the data of summertime (May to October) in the period 1997–2014. First, the daily anomalies of both the observations and model simulations were obtained by the removal of the climatological annual cycle (annual mean plus the three leading harmonics) and the synoptic fluctuations via a 5-day running mean calculated over all years of the data. Then, a bandpass filter (Duchon 1979) at 30–70 days was applied to the daily

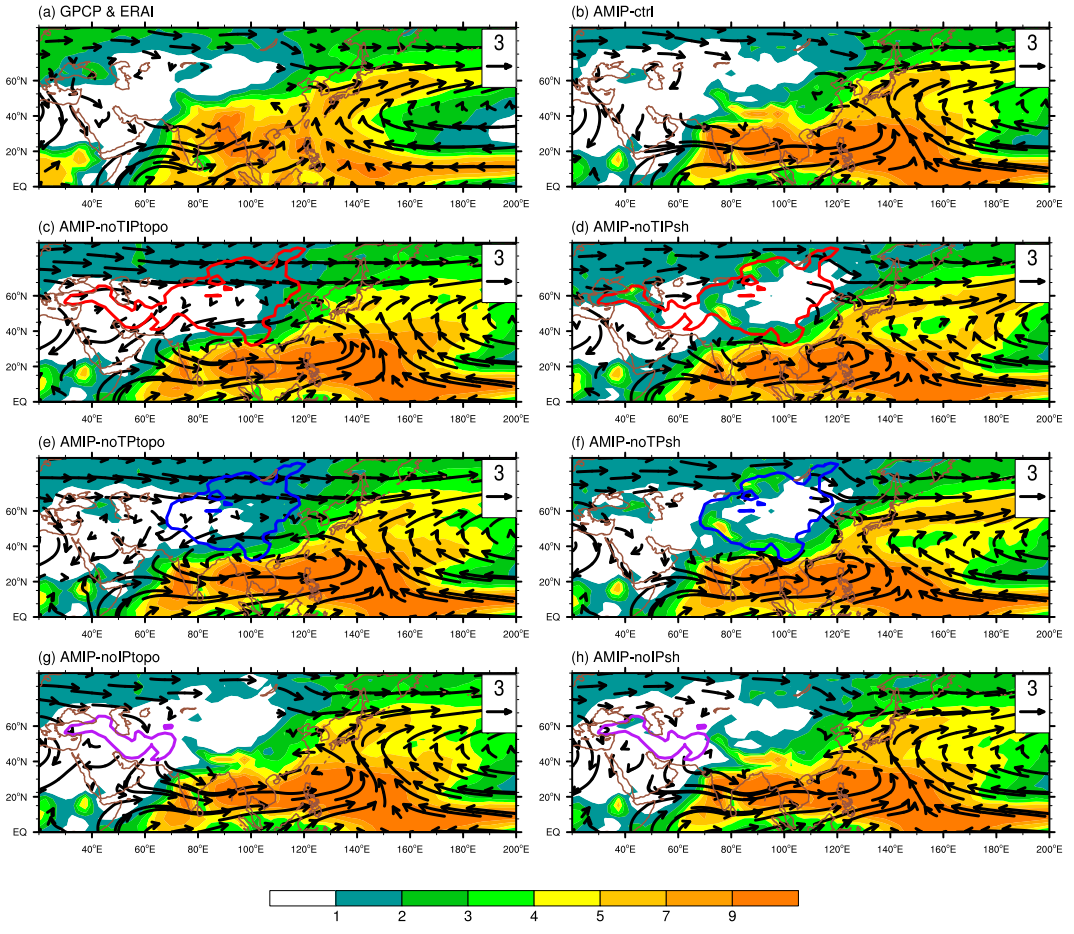

FIG. 2. Climate mean May–October precipitation (shading; mm day^{-1}) and 850-hPa horizontal winds (vectors; m s^{-1}) during 1997–2014 derived from (a) GPCP and ERA-Interim, (b) AMIP-ctrl, and sensitivity experiments without topography or sensible heating over the (c),(d) TIP (red contours), (e),(f) TP (blue contours), and (g),(h) IP (purple contours).

anomalies to derive the intraseasonal component (see section 3 and Fig. 3). Wavenumber frequency analysis (Fu et al. 2003; Fu and Wang 2004) was used to quantify the meridional propagation characteristics of the BSISO in the present study. Individual spectra for the May–October segment were calculated year by year, and then averaged over 18 years of data. Lag-regression analysis was applied to the bandpass-filtered precipitation to assess the northward propagation of the intraseasonal oscillation (ISO) in the Eastern Hemisphere during boreal summer. The Student's *t* test was applied to obtain the statistical significance of model simulations.

d. Model evaluation

The climatological May–October precipitation and horizontal winds in the lower troposphere derived from GPCP, ERA-Interim, and model simulations are given in Fig. 2. Compared with the observational data (Fig. 2a), the control run (AMIP-ctrl) could capture the basic features of the ASM with more than 4 mm day^{-1} rainfall covering the South Asian continent, the Bay of Bengal (BOB), the South China Sea (SCS), and the western Pacific Ocean. It can also well reproduce the Somali jet, the monsoon trough over the BOB, and the anticyclone over the western North Pacific (Fig. 2b). However, the AMIP-ctrl overestimates the precipitation over the Indian Peninsula, BOB, SCS, and western Pacific Ocean, while a simulated cyclonic circulation is located over SCS so that the anticyclone in the western North Pacific is farther east than the observed. Without TIP/TP topography and surface sensible heating, the main climatological features of ASM change little compared with the control run (Figs. 2c–f), except for the reduced rainfall in the southern slope of TP, northern Indian Peninsula, and northern BOB (Figs. S1a–d in the online supplemental material) as well as the weakened cross-equatorial flow (Figs. 7a–d). Furthermore, the pattern of climate mean rainfall and low-level circulation in boreal summer simulated by AMIP-noIPtopo and AMIP-noIPsh is very similar to that by the control run (Figs. 2g–h).

3. Changes in BSISO features

The observed and simulated wavenumber–frequency spectra for daily precipitation anomaly averaged over 80°–100°E in boreal summer are shown in Fig. 3, which presents the

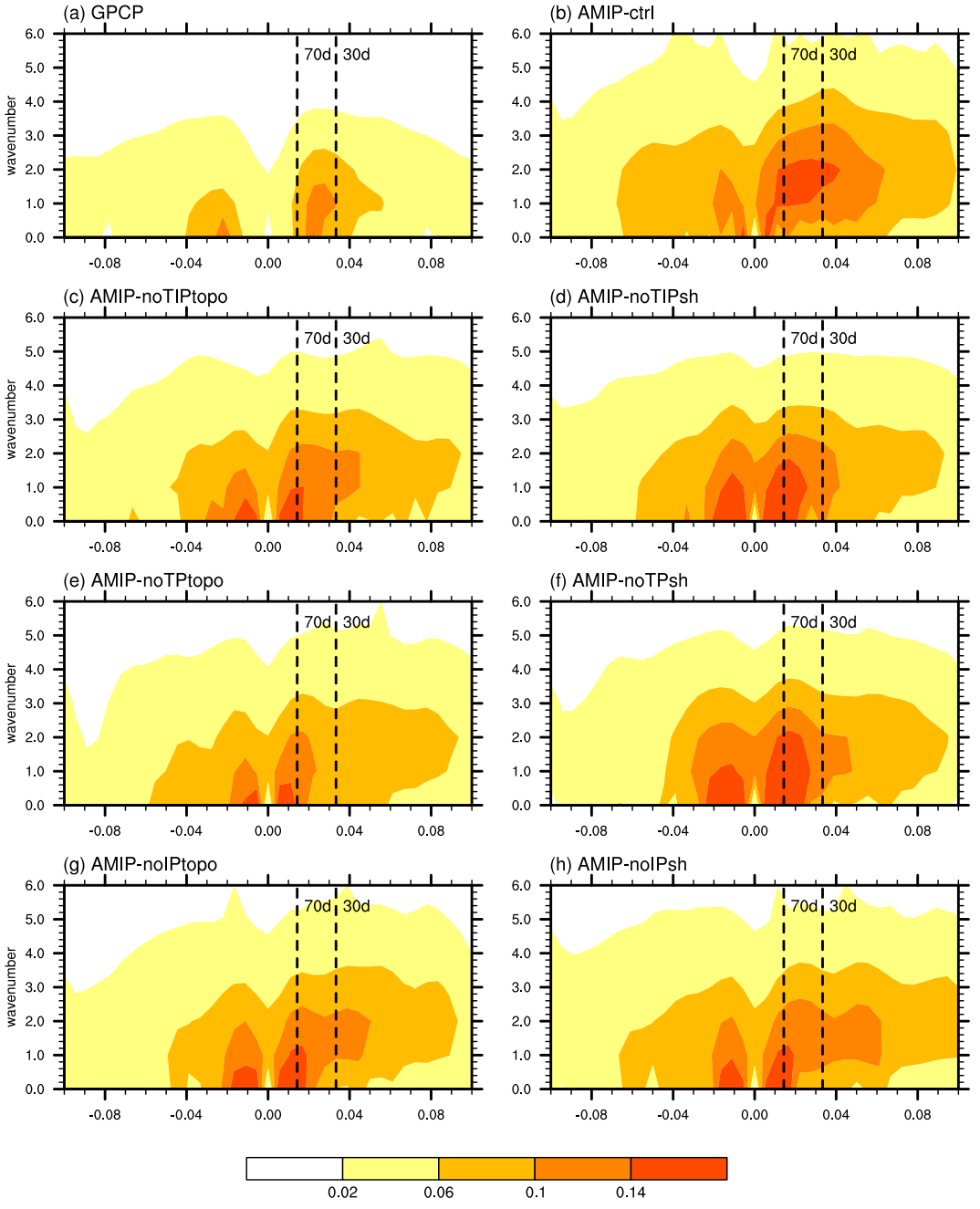

FIG. 3. May–October wavenumber–frequency spectra of daily precipitation anomaly averaged over 80°–100°E (shading; mm^2 day^{-2} per frequency interval per wavenumber interval) derived from (a) GPCP, (b) AMIP-ctrl, (c) AMIP-noTIPtopo, (d) AMIP-noTIPsh, (e) AMIP-noTPtopo, (f) AMIP-noTPsh, (g) AMIP-noIPtopo, and (h) AMIP-noIPsh in the period 1997–2014. Northward propagation is represented by positive frequency and southward propagation by negative frequency.

northward- and southward-propagating disturbances over the Bay of Bengal sector. By definition, northward propagation is represented by positive frequency, and vice versa for southward propagation. Observationally (Fig. 3a), the northward-propagating disturbances clearly dominate over their southward counterparts, for which the maximum spectrum reaches approximately 0.12 (mm^2 day^{-2} per frequency interval per wavenumber interval). The power of northward-propagating disturbances is concentrated at 30–70-day periods and zonal wavenumber 1 for precipitation. The spatiotemporal features of meridionally propagating disturbances are simulated well by the AMIP-ctrl (Fig. 3b). Although the northward power

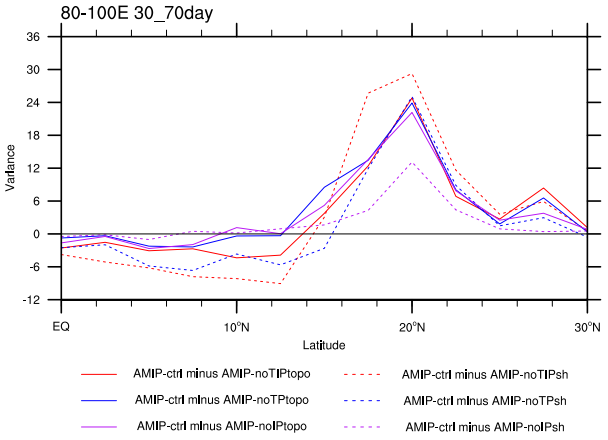

FIG. 4. Differences in the variance of 30–70-day filtered daily precipitation (mm^2 day^{-2}) averaged over 80°–100°E between the control run (AMIP-ctrl) and the six sensitivity tests in boreal summer.

reproduced by AMIP-ctrl is greater than that in observations, the results of the control run also indicate that the distinct northward propagation does occur in boreal summer, especially on the 30–70-day intraseasonal scale. However, all the sensitivity experiments show the intensities of the northward and southward power to be almost the same magnitude, while the northward-propagating component maxima are mainly concentrated on the time scale of lower frequencies than observed (Figs. 3c–h). This indicates that both the reduced orography and the eliminated surface sensible heat within the TIP, TP, or IP region could induce the weakening of the northward component and the shift of the main period of northward-propagating components to lower frequencies during the boreal summer.

As demonstrated by the observed wavenumber-frequency spectra, it is evident that the 30–70-day band is the main oscillation period. Thus, a 30–70-day bandpass filter was further applied to the daily anomalies of precipitation, relative vorticity, and horizontal moisture convergence, to reveal the responses of ISO features to the changes in topography and surface thermal condition in the TIP, TP, or IP region and the associated possible causes. Similar to the model bias in climatological precipitation, the difference in the variance of 30–70-day filtered daily precipitation between AMIP-ctrl and GPCP exists in the latitude band of 15°–20°N along 80°–100°E (Fig. S2). Figure 4 presents the differences in the intraseasonal variance of boreal summer precipitation between AMIP-ctrl and the six sensitivity tests averaged over 80°–100°E. The differences in variance show negative values south of 15°N but positive values north of 15°N, and reach their maxima at 20°N. The summertime ISO intensity is weakened at higher latitudes near the southern TP with the reduced topography or eliminated surface sensible heat in the TIP/TP/IP region. As the longitudinal band of 80°–100°E is the active area of strong northward-propagating ISO, it also indicates the intensity of northward-propagating ISO is decreased. It corresponds well to the results shown by the wavenumber–frequency spectra analyses (Figs. 3c–h). In contrast, the intraseasonal variance in precipitation simulated by AMIP-noIPsh is closest to the control run.

To provide a more direct view of the impacts of the TIP, TP, and IP on the northward propagation of summertime ISO, Fig. 5 presents the meridional propagation of 30–70-day filtered rainfall within the BOB sector (averaged over 80°–100°E), based on the lag regression for both GPCP data and the seven experiments against the reference point (10°N, 85°E) at time lags from day −30 to day 30. Note that only the precipitation from May to October was adopted for the lag-regression calculation, and the amplitudes of regressed rainfall were determined by both the regression coefficients and one standard deviation of bandpass-filtered precipitation. In the GPCP data, a systematic northward propagation starting from the equatorial Indian Ocean to the southern slope of the TP can be clearly seen (Fig. 5a). The Hovmöller diagrams of summertime intraseasonal rainfall along the BOB sector year by year also show strong cases of northward-propagating intraseasonal precipitation can reach south of the TP (Fig. S3). The AMIP-ctrl reproduces this significant northward propagation of ISO rainfall, but with weaker magnitude and a slower phase speed compared with the observed (Fig. 5b). However, the experiments with reduced topography over TIP and TP (AMIP-noTIPtopo and AMIP-noTPtopo) simulate weaker northward propagation of ISO than AMIP-ctrl, especially at higher latitudes (Figs. 5c,e). In AMIP-noTIPsh and AMIP-noTPsh, the ISO rainfall even shows the characteristics of southward propagation in the region north of 20°N (Figs. 5d,f). This confirms that both the topography and surface thermal condition of the TIP/TP influence the northward propagation of ISO to higher latitudes, especially near the southern slope of the TP. However, the effect of TIP/TP sensible heating on the BSISO northward propagation in equatorial and near-equatorial regions is still uncertain and needs further exploration. Compared with TP, the IP has a limited effect on the northward propagation of ISO rainfall both dynamically and thermally (Figs. 5g,h).

4. Causes of the changes in the northward propagation of the BSISO

Alteration of the large-scale topographic height and surface thermal condition will inevitably cause changes in the climatological circulation and water vapor transport. Therefore, the differences between the control run (AMIP-ctrl) and six sensitivity tests in terms of circulation and water vapor during boreal summer are first analyzed, indicating the dynamic and thermal effects of the TIP, TP, and IP on the mean state. Figure 6 illustrates the differences in May–October mean air temperature and wind fields in the upper level with and without the topography or surface sensible heating over the TIP, TP, and IP. The presence of TIP topography could stimulate a warm anticyclone in the upper troposphere with a maximum center of air temperature located on the IP side. Meanwhile, significant easterly anomalies at the southern branch of the anticyclone can also be found in the latitudinal band of 10°–30°N (Fig. 6a). In contrast, the anticyclonic circulation

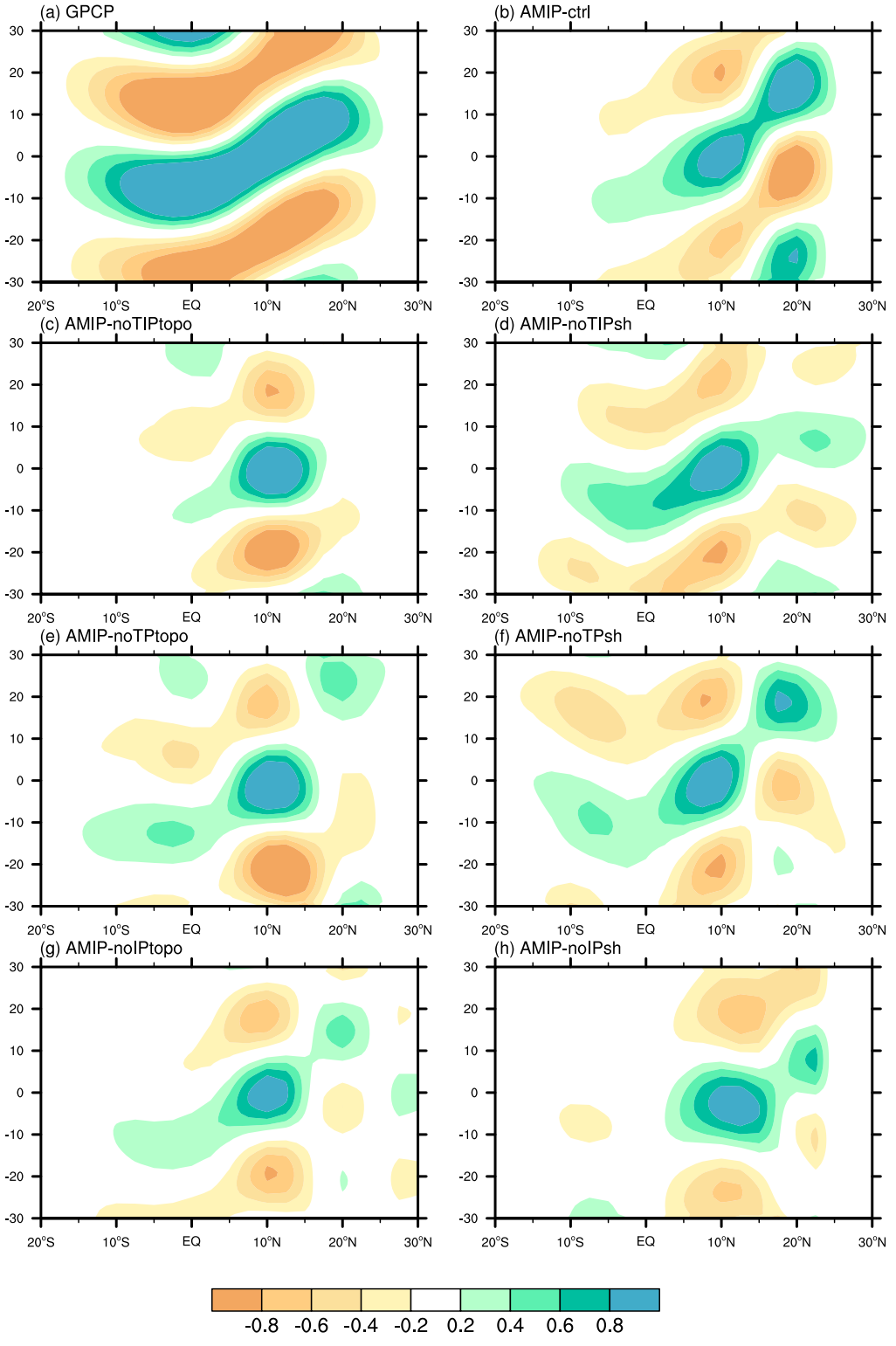

FIG. 5. Latitude–time evolution of intraseasonal precipitation as depicted by the lag regression of the 30–70-day bandpass-filtered rainfall anomaly (shading; mm day^{-1}) averaged over 80°–100°E obtained from (a) GPCP and the seven experiments: (b) AMIP-ctrl, (c) AMIP-noTIPtopo, (d) AMIP-noTIPsh, (e) AMIP-noTPtopo, (f) AMIP-noTPsh, (g) AMIP-noIPtopo, and (h) AMIP-noIPsh during boreal summer (May–October). The ISO precipitation at 10°N, 85°E was used as a reference point for calculating the lag regression. Only those values of precipitation that are statistically significant at the 95% confidence level are plotted.

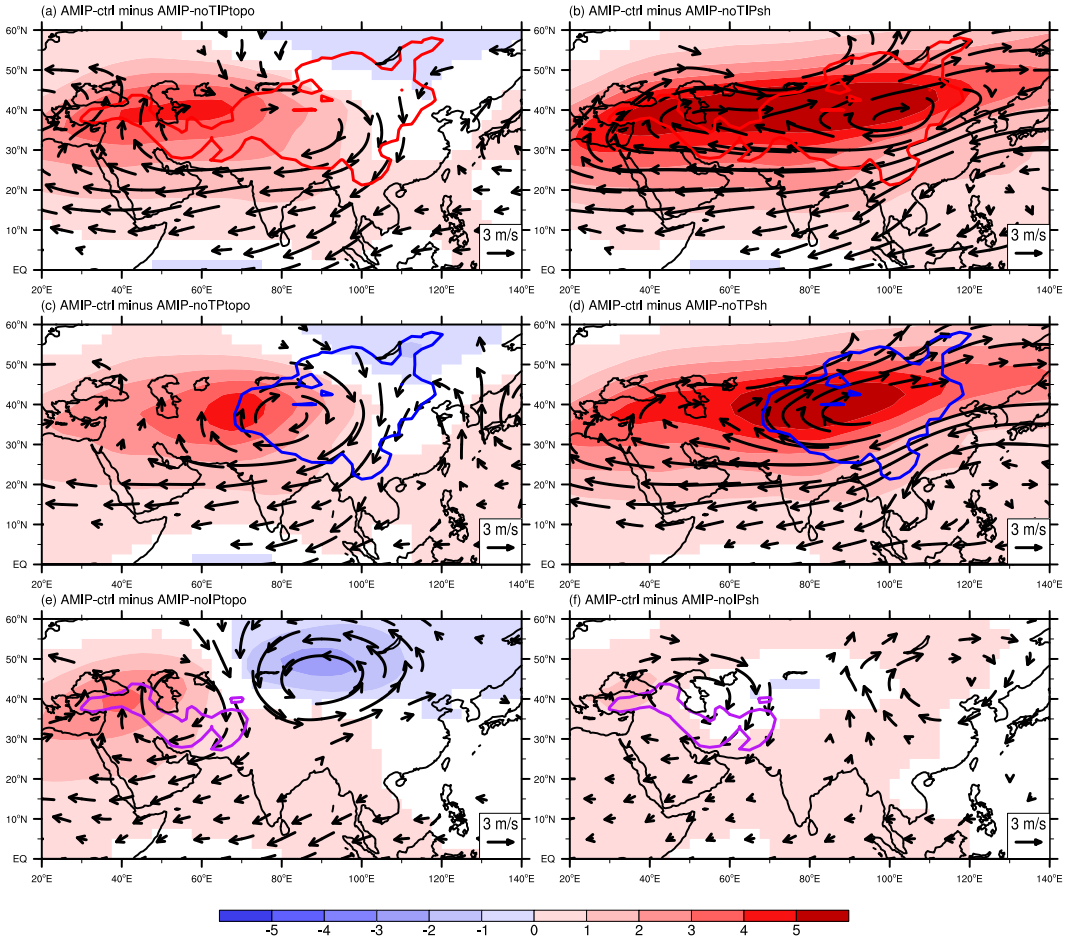

FIG. 6. Differences in May–October mean air temperature (shading; K) and winds (vectors; m s^{-1}) at 200 hPa between AMIP-ctrl and six sensitivity experiments without topography or surface sensible heating over the (a),(b) TIP (red contour), (c),(d) TP (blue contour), and (e),(f) IP (purple contour). Only those values of air temperature and winds (at least one component) that are statistically significant at the 95% confidence level are plotted.

and warm center induced by the TIP sensible heating are not only much stronger but also cover a larger area. Likewise, the existence of TIP sensible heating also causes the upper-level easterly wind anomalies over the ASM region (Fig. 6b). This indicates that the combined effects of TIP sensible heating generate an enhanced warm anticyclone in the upper layer, which is consistent with the results of Liu et al. (2017). The warm anticyclonic center in the upper level induced by the TP terrain is located on the TP side (Fig. 6c), while the intensity and range of warm anticyclone caused by TP thermal forcing are smaller than those by TIP (Fig. 6d vs Fig. 6b). The IP topography, however, could induce a dipole pattern of upper-tropospheric temperature with a positive anomaly on the western IP and a negative anomaly on the north of TP, corresponding to an anticyclone and a cyclone, respectively (Fig. 6e). In contrast, the thermal forcing of IP has a minimum impact on the upper-level circulation among the six sensitivity experiments (Fig. 6f). Compared with the TP, the dynamic and thermal effects of IP have less influence on the upper-level circulation over the ASM region.

Figure 7 presents the distribution of difference in moisture and lower-tropospheric horizontal winds between the control run and six sensitivity experiments. In the presence of TIP/TP topography, positive anomalies of specific humidity are mainly located over South Asia, the northern Indian Ocean, and East China, and negative anomalies over northern Eurasia and northern Africa. These positive moisture anomalies are closely related to the cross-equatorial flow that brings water vapor from the southern Indian Ocean (Figs. 7a,c). The pattern of differences with and without surface sensible heat over TIP/TP is similar to that by terrain experiments in the same region, but with greater intensity (Figs. 7b,d). The IP topography also causes the positive moisture anomaly over South Asia accompanied with an anomalous cross-equatorial flow (Fig. 7e); however, the IP surface sensible heating induces little change in water vapor and low-level wind field (Fig. 7f).

To further explore the change in water vapor transport caused by the dynamic and thermal effects of the TIP, TP, and IP, Fig. 8 shows the differences in May–October mean

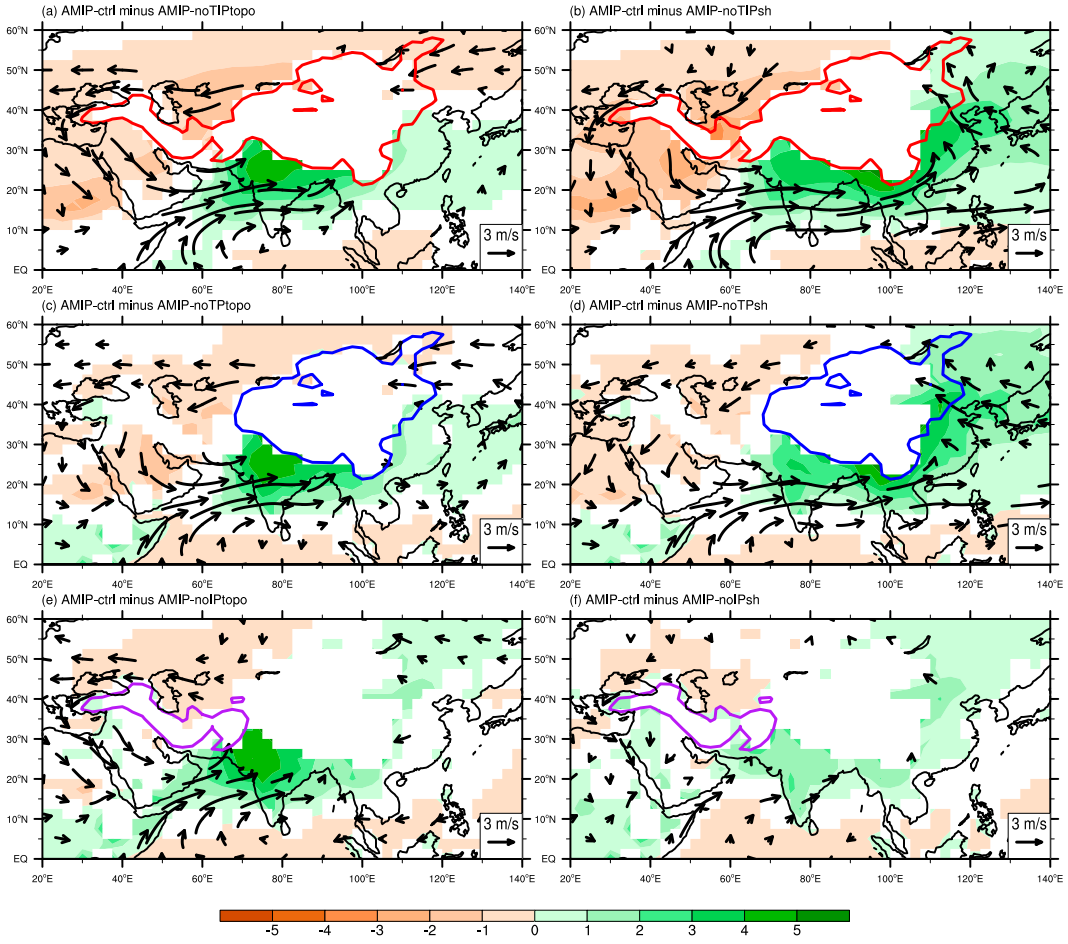

FIG. 7. As in Fig. 6, but for specific humidity (shading; g kg^{-1}) and the wind field (vectors; m s^{-1}) at 850 hPa. Only those values of specific humidity and winds (at least one component) that are statistically significant at the 95% confidence level are plotted.

vertically integrated moisture flux and its convergence from the surface to 100 hPa between the control run and six sensitivity tests. The dynamic and thermal effects of TIP/TP cause the moisture to accumulate in South Asia and the northern Bay of Bengal, while a large area of water vapor flux divergence occurs in the near-equatorial Indian Ocean (shading in Figs. 8a–d). The IP dynamic effect on water vapor convergence is similar to the effects of TP (Fig. 8e), but the IP thermal effect on moisture convergence is much smaller (Fig. 8f). The patterns of moisture convergence difference correspond well to that of rainfall difference presented in Fig. S1. Accordingly, the above large centers of convergence and divergence are linked by strong cross-equatorial water vapor flux anomalies that bring large amounts of moisture from the ocean to the ASM region (vectors in Figs. 8a–e). The abundant moisture supply to the ASM region induced by TIP/TP dynamic and thermal effects will create a favorable background for the occurrence of local systematic convection.

According to the above analyses, the climate mean background fields, such as vertical zonal wind shear and the meridional specific humidity gradient, are definitely influenced by the TIP/TP dynamical and thermal effects, which are of paramount importance in the northward propagation of ISO during boreal summer. Subsequently, we examined the climatological May–October mean zonal winds and vertical shear, as well as the specific humidity, averaged over 80°–100°E in the ERA-Interim data and model simulations (Fig. 9). The vertical zonal wind shear is defined as the differences in zonal winds between 200 and 850 hPa (former minus the latter, $U_{200} - U_{850}$). The easterly vertical wind shear (negative value) in the observed data appears from the equator to 24°N and reaches its minimum near 5°N (see black solid line in Fig. 9c). The AMIP-ctrl (black dashed line) simulates the easterly vertical wind shear well, but with larger magnitude. The zonal wind shear simulated by two IP experiments (purple lines) is similar to that by AMIP-ctrl. However, the ranges of easterly shear simulated by the four sensitivity tests related to TIP/TP experiments (red and blue lines) are smaller than the observed and AMIP-ctrl results, as the point where the difference in zonal winds is zero occurs at approximately 20°N or less (Fig. 9c). The weakened easterly shear simulated by AMIP-noTIPtopo, AMIP-noTIPsh, AMIP-noTPtopo, and

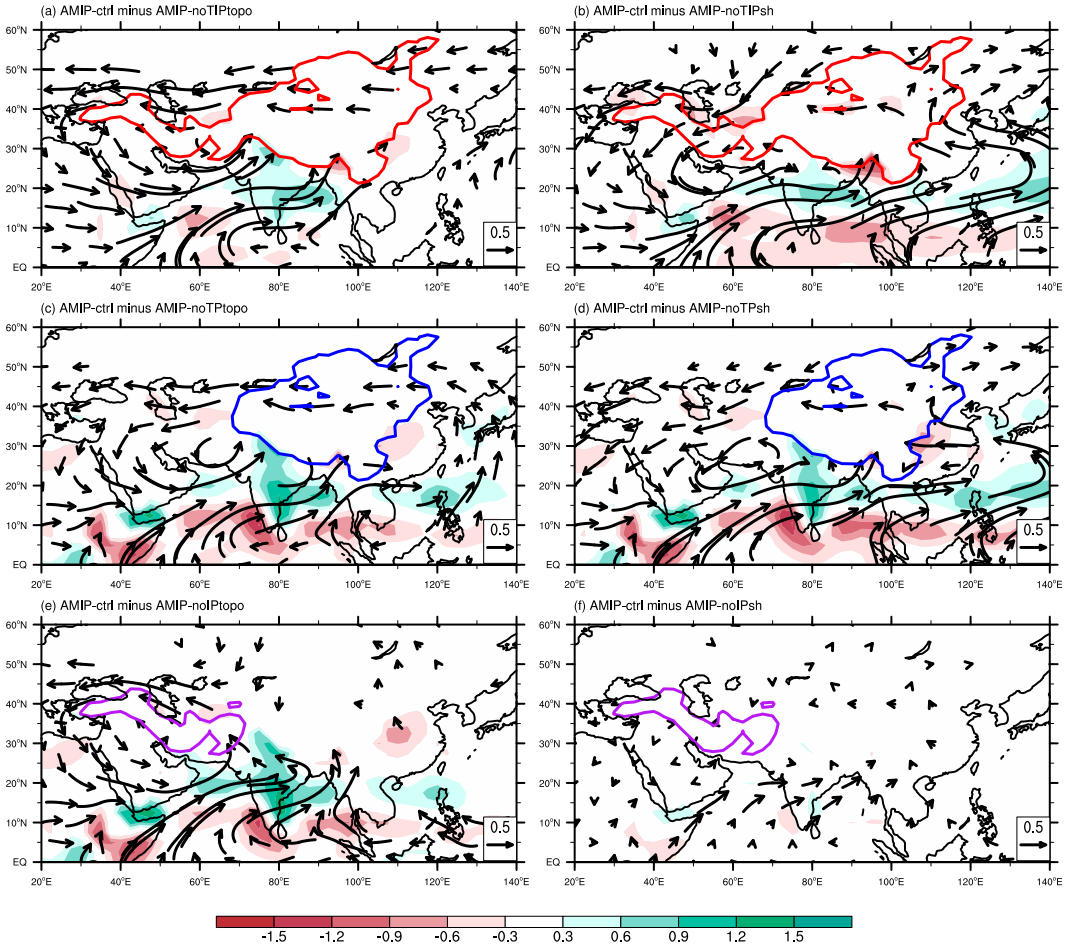

FIG. 8. As in Fig. 6, but for vertically integrated moisture flux (vectors; kg m^{-1} s^{-1}) and moisture flux convergence (shading; 10^{-6} kg m^{-2} s^{-1}) from the surface to 100 hPa. Only those values of moisture flux convergence and moisture flux (at least one component) that are statistically significant at the 95% confidence level are plotted.

AMIP-noTPsh is attributable to both the weakened easterlies in the upper troposphere (Fig. 9a) and reduced westerly winds in the lower troposphere, especially to the north of 15°N (Fig. 9b). This implies thermodynamic effects of the TIP/TP on the strength of zonal winds and, subsequently, the range of vertical easterly shear. Wu et al. (2016, 2017) revealed the mechanism of the surface sensible heating over TP affecting easterly wind shear over the ASM region based on both the observational analysis and model sensitivity tests. The TP sensible heating can induce minimum absolute vorticity and potential vorticity near the tropopause above the TP via changing the atmospheric thermal structure. Subject to angular momentum conservation, a strong subtropical monsoonal-type meridional circulation is thus generated with lower-layer southerlies and higher-layer northerlies. According to the principle of geostrophic wind and thermal wind balance, easterly (westerly) winds occur in the upper (lower) troposphere, resulting in easterly vertical wind shear.

Furthermore, the lack of terrain or sensible heating in the TIP/TP/IP region also affects the meridional gradient of mean specific humidity (Fig. 9d). The meridional profiles of mean specific humidity in the observations and AMIP-ctrl show positive meridional gradients to the south of 15°N, which benefit the northward shift of convective heating, whereas the moisture maxima in the six sensitivity experiments are located at about 10°N. This indicates that the negative meridional gradients of moisture are located to the north of 10°N in the six sensitivity tests. Therefore, both the narrowed range of easterly shear and the negative meridional specific humidity gradients located in the northern Bay of Bengal are caused by the reduced topography or eliminated sensible heating in the TIP/TP region, which are not conducive to ISO northward propagation.

Against the background of the vertical easterly shear of the mean flow, the key mechanism responsible for the northward propagation of ISO is the generation of a strong positive barotropic vorticity anomaly located to the north of the ISO's convective center, due to the coupling between the baroclinic and barotropic modes in the free atmosphere (Wang and Xie 1997; Jiang et al. 2004). Thus, we examined the latitude–pressure

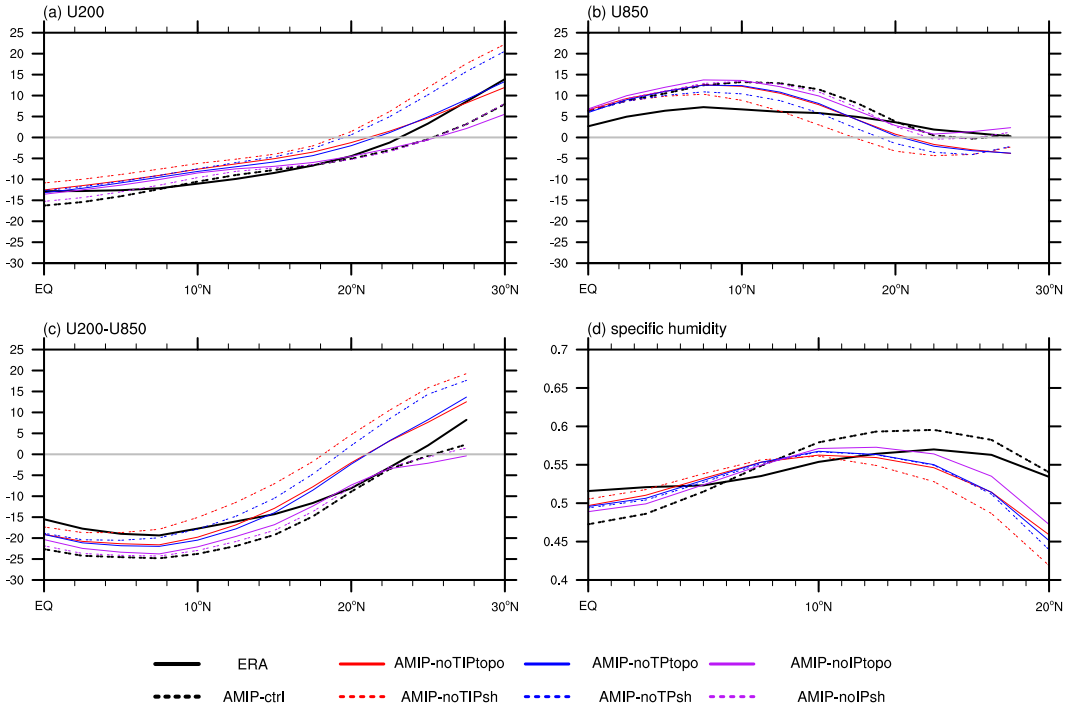

FIG. 9. Meridional structures of May–October mean (a) U_{200} (m s^{-1}), (b) U_{850} (m s^{-1}), (c) zonal shear (m s^{-1}), and (d) vertically integrated specific humidity (kg m^{-2}) from the surface to 100 hPa averaged over 80°–100°E from ERA-Interim data and model simulations.

structures of regressed ISO relative vorticity averaged over 80°–100°E with respect to the ISO rainfall at the reference point (20°N, 90°E) in the observations and model simulations (Figs. 10 and 11a–d). The observations show that a strong positive anomaly of relative vorticity with barotropic structure is located to the north of the ISO rainfall center (Fig. 10a). Three experiments (AMIP-ctrl, AMIP-noIPtopo, and AMIP-noIPsh) could successfully reproduce the observed structure of vorticity, albeit with the first two showing slightly larger magnitude (Figs. 10b and 11c,d). However, the centers of filtered relative vorticity correspond exactly to the centers of ISO precipitation in AMIP-noTIPtopo, AMIP-noTPtopo, and AMIP-noTPsh (Figs. 10c and 11a,b), while the vorticity center in AMIP-noTIPsh is located south of the rainfall center (Fig. 10d). This indicates that the contraction of the simulated easterly shear region (Fig. 9c) restricts the generation of positive vorticity with barotropic structure north of 20°N, thus impeding the ISO's propagation to the northern Bay of Bengal in the TIP/TP sensitivity experiments.

Furthermore, positive barotropic vorticity to the north of the convective center will lead to PBL moisture convergence that favors the formation of new convection, and thus the ISO convection propagates northward (Jiang et al. 2004). In addition, the mean meridional gradient of specific humidity may contribute to the generation of PBL moisture convergence to the north of the ISO convective center through moisture advection (DeMott et al. 2013). Accordingly, cross sections of regressed ISO horizontal moisture divergence from observations and the simulations were also produced (Figs. 10 and 11e–h). In the observations, a maximum of moisture convergence in the PBL is concentrated around the convective center, showing a northward extension (Fig. 10e). The PBL moisture convergence is simulated well in AMIP-ctrl and AMIP-noIPsh, and its pattern is similar to the observed one but with stronger intensity (Figs. 10f and 11h). In contrast, the moisture convergence centers in the TIP/TP sensitivity experiments are located to the south of the ISO convection, which is consistent with the failure to reproduce the barotropic vorticity to the north of the convective heating (Figs. 10g,h and 11e,f).

In general, the topographic uplift or surface sensible heat over the TIP/TP effectively maintains the easterly vertical shear and positive meridional gradient of water vapor, especially over the northern BOB, creating the background conditions for the generation of positive barotropic vorticity and PBL moisture convergence to the north of the ISO convective center. Subsequently, this induces the ISO to propagate as far north as the southern slope of the TP. Because the effects of IP have little influence on the zonal wind shear dynamically and thermally, the northward propagation characteristics of BSISO simulated by IP sensitivity experiments are not much different from that by AMIP-ctrl.

Since the AMIP experiments were used for comparative analyses, the role of air–sea interaction was not examined in our study. Figure S4 in the online supplemental material shows that there is no change in surface sea temperature between the control run and the six sensitivity experiments. Thus, our study indicates that from the perspective of internal

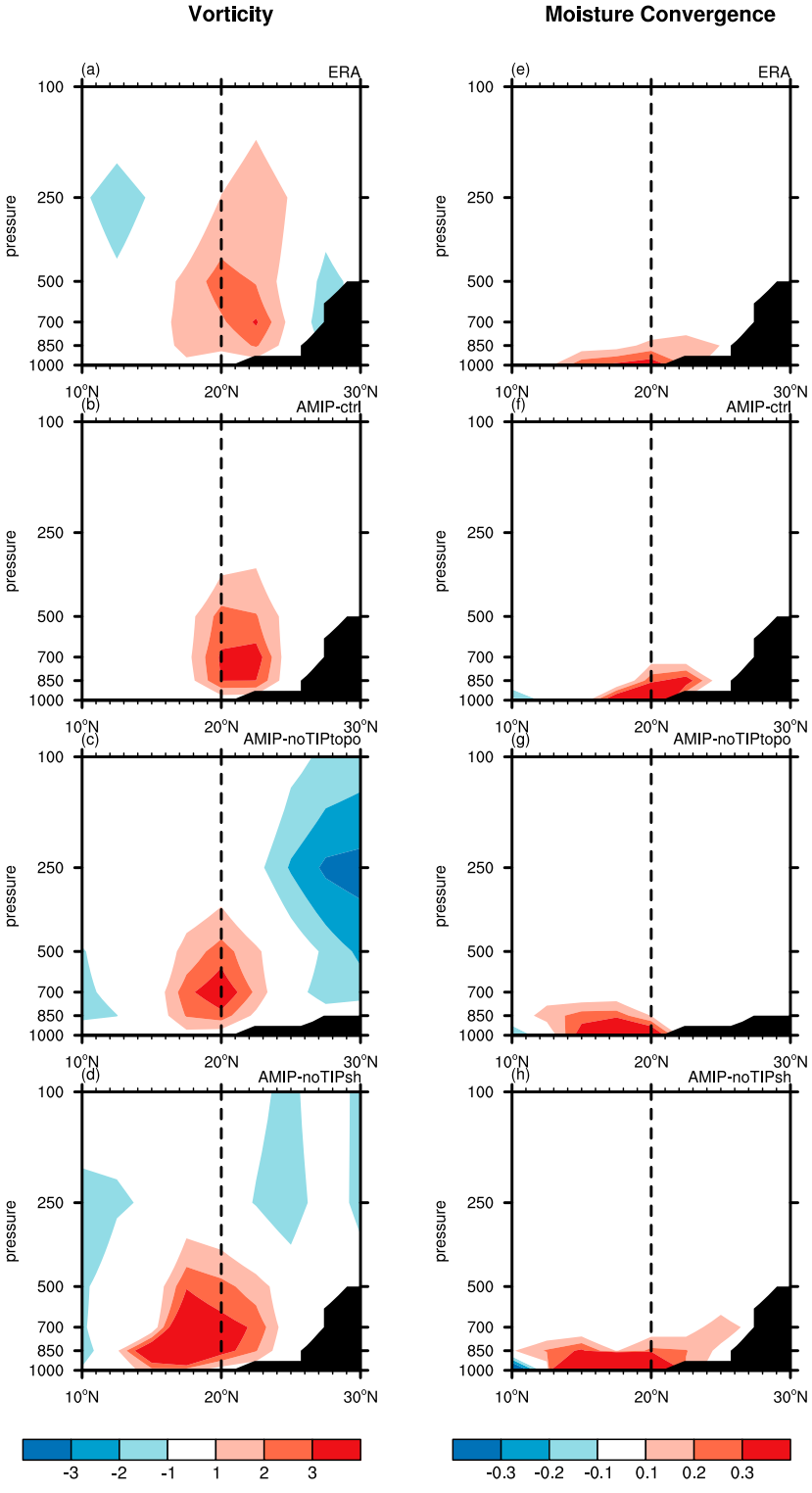

FIG. 10. Meridional–vertical structures of regressed 30–70-day filtered (a)–(d) relative vorticity (10^{-6} s^{-1}) and (e)–(h) moisture convergence (10^{-10} kg kg^{-1} s^{-1}) averaged over 80°–100°E from (a),(e) ERA-Interim, (b),(f) AMIP-ctrl, (c),(g) AMIP-noTIPtopo, and (d),(h) AMIP-noTIPsh. The 30–70-day filtered precipitation anomaly at 20°N, 90°E was used as a reference for calculating the regressions. Black shading represents the terrain height. Only those values that are statistically significant at the 95% confidence level are plotted.

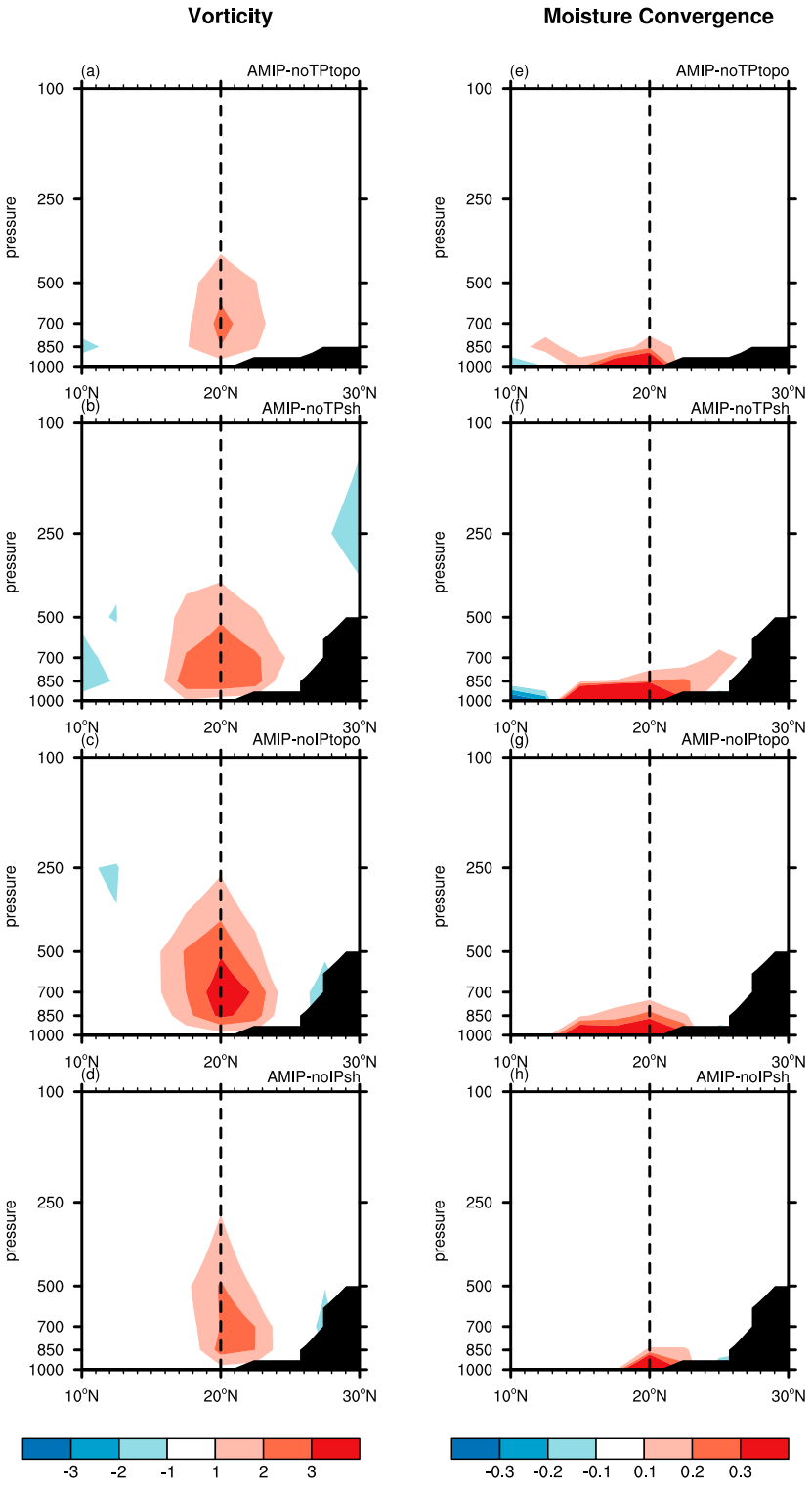

FIG. 11. As in Fig. 10, but for (a),(e) AMIP-noTPtopo, (b),(f) AMIP-noTPsh, (c),(g) AMIP-noIPtopo, and (d),(h) AMIP-noIPsh.

atmospheric dynamic processes, the most significant changes in BSISO northward propagation are found in the northern BOB after the removal of TIP/TP topography or surface sensible heating. It is consistent with the results derived from a theoretical framework constructed by Jiang et al. (2004), which demonstrates that the internal atmospheric dynamic processes associated with easterly wind shear mainly contributes to the BSISO northward propagation over the off-equatorial area in the Northern Hemisphere, while the air–sea interaction also contributes obviously in the region near the equator.

5. Conclusions and discussion

Based on comparative analyses of the control run and six sensitivity experiments using the atmospheric model component of CAS FGOALS-f3-L, the dynamic and thermal effects of the TIP on the characteristics of the northward-propagating BSISO were investigated in this study, as well as the relative importance of the TP and IP to the northward propagation of BSISO. Then, the physical mechanisms responsible for the changes in the northward propagation of the BSISO were further explored from the viewpoint of circulation and water vapor transport.

The control run (AMIP-ctrl) performed by CAS FGOALS-f3-L reproduces the spatiotemporal characteristics of the northward-propagating BSISO rainfall well in the Bay of Bengal sector, albeit with a slightly slower phase speed. However, both reduced terrain height and eliminated surface sensible heat within the TIP, TP, or IP region weaken the northward component and induce a shift in the main period to lower frequencies. In addition, these changes in characteristics of TIP/TP influence the northward propagation of the BSISO to higher latitudes, especially near the southern slope of the TP. However, the dynamic and thermal effects of the IP on the northward propagation of BSISO are limited compared with those of the TP.

The maintenance of TIP/TP surface sensible heat stimulates a warm anticyclone in the upper troposphere, of which the southern branch presents significant easterly anomalies over the ASM region. Meanwhile, it benefits the moisture convergence over South Asia and the northern Bay of Bengal, mainly transported from the equatorial Indian Ocean, accompanied by obvious westerly anomalies over the ASM region in the lower troposphere. Similar feedback of the circulation and water vapor condition can also be caused by the presence of TIP/TP topography. It is illustrated that without the terrain or surface sensible heat within the TIP/TP, the magnitude of easterly vertical wind shear is weakened and the range is narrowed, while a negative meridional specific humidity gradient occurs in the northern Bay of Bengal. These alterations of mean state restrict the generation of positive vorticity with barotropic structure together with PBL moisture convergence to the north of the ISO convective center, thus impeding the ISO's northward propagation. This means that the TIP/TP directly influences the surrounding circulation and water vapor distribution via its dynamic and thermal effects, and then modulates the northward propagation of the BSISO in the northern Bay of Bengal. In contrast, the IP dynamic and thermal effects on the background circulation and water vapor convergence are very limited, so the TP plays a decisive role in the BSISO northward propagation.

On the interannual to interdecadal time scales, the TP is not only an important forcing source for affecting global oceanic circulations, but it is also influenced by remote oceans via the Rossby waves, westerly jet, local atmospheric response, and teleconnections (Cui et al. 2015; Hu and Duan 2015; He et al. 2019a). There are few studies on the interaction between the plateaus and the oceans on an intraseasonal time scale. In addition, DeMott et al. (2013) pointed out that air–sea interaction is the second most important mechanism after PBL moisture advection and easterly wind shear for the ISO's northward propagation. Therefore, it is necessary to conduct similar studies but using coupled models to examine the complex interactions between TIP and Indian Ocean on the intraseasonal time scale and their synergistic effect on the activity of ISO. Furthermore, we only focused on the TIP's effects on the northward propagation of the BSISO in the Indian Ocean. Given that significant BSISO northward propagation also occurs over the WNP-EA, and the corresponding mechanisms are different, further research concentrated on the WNP-EA region will be performed in the future.

Acknowledgments. This work was jointly supported by the National Natural Science Foundation of China (41730963), the Strategic Priority Research Program of the Chinese Academy of Sciences (XDB40030204), and the National Natural Science Foundation of China (41875076 and 41775047).

REFERENCES

Bolin, B., 1950: On the influence of the Earth's orography on the general character of the westerlies. *Tellus*, **2**, 184–195, https://doi.org/10.3402/tellusa.v2i3.8547.

Boos, W. R., and Z. M. Kuang, 2010: Dominant control of the South Asian monsoon by orographic insulation versus plateau heating. *Nature*, **463**, 218–222, https://doi.org/10.1038/nature08707.

Cui, Y. F., A. M. Duan, Y. M. Liu, and G. X. Wu, 2015: Interannual variability of the spring atmospheric heat source over the Tibetan Plateau forced by the North Atlantic SSTA. *Climate Dyn.*, **45**, 1617–1634, https://doi.org/10.1007/s00382-014-2417-9.

Dee, D. P., and Coauthors, 2011: The ERA-Interim reanalysis: Configuration and performance of the data assimilation system. *Quart. J. Roy. Meteor. Soc.*, **137**, 553–597, https://doi.org/10.1002/qj.828.

DeMott, C. A., C. Stan, and D. A. Randall, 2013: Northward propagation mechanisms of the boreal summer intraseasonal oscillation in the ERA-Interim and SP-CCSM. *J. Climate*, **26**, 1973–1992, https://doi.org/10.1175/JCLI-D-12-00191.1.

Ding, Q., and B. Wang, 2009: Predicting extreme phases of the Indian summer monsoon. *J. Climate*, **22**, 346–363, https://doi.org/10.1175/2008JCLI2449.1.

Duan, A. M., and G. X. Wu, 2005: Role of the Tibetan Plateau thermal forcing in the summer climate patterns over subtropical Asia. *Climate Dyn.*, **24**, 793–807, https://doi.org/10.1007/s00382-004-0488-8.

——, D. Hu, W. Hu, and P. Zhang, 2020: Precursor effect of the Tibetan Plateau heating anomaly on the seasonal march of the East Asian summer monsoon precipitation. *J. Geophys. Res. Atmos.*, **125**, e2020JD032948, https://doi.org/10.1029/2020JD032948.

Duchon, C. E., 1979: Lanczos filtering in one and two dimensions. *J. Appl. Meteor.*, **18**, 1016–1022, https://doi.org/10.1175/1520-0450(1979)018<1016:LFIOAT>2.0.CO;2.

Flohn, H., 1957: Large-scale aspects of the "summer monsoon" in South and East Asia. *J. Meteor. Soc. Japan*, **35**, 180–186, https://doi.org/10.2151/jmsj1923.35A.0_180.

Fu, X., and B. Wang, 2004: Differences of boreal summer intraseasonal oscillations simulated in an atmosphere–ocean coupled model and an atmosphere-only model. *J. Climate*, **17**, 1263–1271, https://doi.org/10.1175/1520-0442(2004)017<1263:DOBSIO>2.0.CO;2.

——, ——, T. Li, and J. P. McCreary, 2003: Coupling between northward-propagating, intraseasonal oscillations and sea surface temperature in the Indian Ocean. *J. Atmos. Sci.*, **60**, 1733–1753, https://doi.org/10.1175/1520-0469(2003)060<1733:CBNIOA>2.0.CO;2.

Goswami, B. N., R. S. Ajayamohan, P. K. Xavier, and D. Sengupta, 2003: Clustering of synoptic activity by Indian summer monsoon intraseasonal oscillations. *Geophys. Res. Lett.*, **30**, 1431, https://doi.org/10.1029/2002GL016734.

He, B., Y. Liu, G. Wu, Z. Wang, and Q. Bao, 2019a: The role of air–sea interactions in regulating the thermal effect of the Tibetan–Iranian Plateau on the Asian summer monsoon. *Climate Dyn.*, **52**, 4227–4245, https://doi.org/10.1007/s00382-018-4377-y.

——, and Coauthors, 2019b: CAS FGOALS-f3-L model datasets for CMIP6 historical Atmospheric Model Intercomparison Project simulation. *Adv. Atmos. Sci.*, **36**, 771–778, https://doi.org/10.1007/s00376-019-9027-8.

——, and Coauthors, 2020: CAS FGOALS-f3-L model datasets for CMIP6 GMMIP tier-1 and tier-3 experiments. *Adv. Atmos. Sci.*, **37**, 18–28, https://doi.org/10.1007/s00376-019-9085-y.

Held, I. M., M. Ting, and H. Wang, 2002: Northern winter stationary waves: Theory and modeling. *J. Climate*, **15**, 2125–2144, https://doi.org/10.1175/1520-0442(2002)015<2125:NWSWTA>2.0.CO;2.

Hsu, H.-H., and X. Liu, 2003: Relationship between the Tibetan Plateau heating and East Asian summer monsoon rainfall. *Geophys. Res. Lett.*, **30**, 2066, https://doi.org/10.1029/2003GL017909.

——, C. Weng, and C. Wu, 2004: Contrasting characteristics between the northward and eastward propagation of the intraseasonal oscillation during the boreal summer. *J. Climate*, **17**, 727–743, https://doi.org/10.1175/1520-0442(2004)017<0727:CCBTNA>2.0.CO;2.

Hsu, P.-C., J.-Y. Lee, and K.-J. Ha, 2016: Influence of boreal summer intraseasonal oscillation on rainfall extremes in southern China. *Int. J. Climatol.*, **36**, 1403–1412, https://doi.org/10.1002/joc.4433.

——, ——, ——, and C.-H. Tsou, 2017: Influences of boreal summer intraseasonal oscillation on heat waves in monsoon Asia. *J. Climate*, **30**, 7191–7211, https://doi.org/10.1175/JCLI-D-16-0505.1.

Hu, J., and A. M. Duan, 2015: Relative contributions of the Tibetan Plateau thermal forcing and the Indian Ocean sea surface temperature basin mode to the interannual variability of the East Asian summer monsoon. *Climate Dyn.*, **45**, 2697–2711, https://doi.org/10.1007/s00382-015-2503-7.

Hu, W., A. Duan, Y. Li, and B. He, 2016: The intraseasonal oscillation of eastern Tibetan Plateau precipitation in response to the summer Eurasian wave train. *J. Climate*, **29**, 7215–7230, https://doi.org/10.1175/JCLI-D-15-0620.1.

Huffman, G. J., R. F. Adler, M. Morrissey, D. T. Bolvin, S. Curtis, R. Joyce, B. McGavock, and J. Susskind, 2001: Global precipitation at one-degree daily resolution from multi-satellite observations. *J. Hydrometeor.*, **2**, 36–50, https://doi.org/10.1175/1525-7541(2001)002<0036:GPAODD>2.0.CO;2.

Jiang, X., T. Li, and B. Wang, 2004: Structures and mechanisms of the northward propagating boreal summer intraseasonal oscillation. *J. Climate*, **17**, 1022–1039, https://doi.org/10.1175/1520-0442(2004)017<1022:SAMOTN>2.0.CO;2.

Kang, I.-S., D. Kim, and J.-S. Kug, 2010: Mechanism for northward propagation of boreal summer intraseasonal oscillation: Convective momentum transport. *Geophys. Res. Lett.*, **37**, L24804, https://doi.org/10.1029/2010GL045072.

Kemball-Cook, S., and B. Wang, 2001: Equatorial waves and air–sea interaction in the boreal summer intraseasonal oscillation. *J. Climate*, **14**, 2923–2942, https://doi.org/10.1175/1520-0442(2001)014<2923:EWAASI>2.0.CO;2.

Kikuchi, K., and B. Wang, 2010: Formation of tropical cyclones in the northern Indian Ocean associated with two types of tropical intraseasonal oscillation modes. *J. Meteor. Soc. Japan*, **88**, 475–496, https://doi.org/10.2151/jmsj.2010-313.

Krishnamurti, T. N., and D. Subrahmanyam, 1982: The 30–50-day mode at 850 mb during MONEX. *J. Atmos. Sci.*, **39**, 2088–2095, https://doi.org/10.1175/1520-0469(1982)039<2088:TDMAMD>2.0.CO;2.

Krishnan, R., C. Zhang, and M. Sugi, 2000: Dynamics of breaks in the Indian summer monsoon. *J. Atmos. Sci.*, **57**, 1354–1372, https://doi.org/10.1175/1520-0469(2000)057<1354:DOBITI>2.0.CO;2.

Lee, J. Y., B. Wang, M. C. Wheeler, X. Fu, D. E. Waliser, and I.-S. Kang, 2013: Real-time multivariate indices for the boreal summer intraseasonal oscillation over the Asian summer monsoon region. *Climate Dyn.*, **40**, 493–509, https://doi.org/10.1007/s00382-012-1544-4.

Li, J. X., Q. Bao, Y. M. Liu, G. X. Wu, L. Wang, B. He, X. C. Wang, and J. D. Li, 2019: Evaluation of FAMIL2 in simulating the climatology and seasonal-to-interannual variability of tropical cyclone characteristics. *J. Adv. Model. Earth Syst.*, **11**, 1117–1136, https://doi.org/10.1029/2018MS001506.

Li, K., Z. Li, Y. Yang, B. Xiang, Y. Liu, and W. Yu, 2015: Strong modulations on the Bay of Bengal monsoon onset vortex by the first northward-propagating intra-seasonal oscillation. *Climate Dyn.*, **47**, 107–115, https://doi.org/10.1007/s00382-015-2826-4.

Li, T., and B. Wang, 1994: The influence of sea surface temperature on the tropical intraseasonal oscillation: A numerical experiment. *Mon. Wea. Rev.*, **122**, 2349–2362, https://doi.org/10.1175/1520-0493(1994)122<2349:TIOSST>2.0.CO;2.

Liu, Y., Z. Wang, H. Zhuo, and G. Wu, 2017: Two types of summertime heating over Asian large-scale orography and excitation of potential-vorticity forcing II. Sensible heating over Tibetan-Iranian Plateau. *Sci. China Earth Sci.*, **60**, 733–744, https://doi.org/10.1007/s11430-016-9016-3.

——, M. Lu, H. Yang, A. Duan, B. He, S. Yang, and G. Wu, 2020: Land–atmosphere–ocean coupling associated with the Tibetan Plateau and its climate impacts. *Natl. Sci. Rev.*, **7**, 534–552, https://doi.org/10.1093/nsr/nwaa011.

Moon, J.-Y., B. Wang, S.-S. Lee, and K.-J. Ha, 2018: An intraseasonal genesis potential index for tropical cyclones during Northern Hemisphere summer. *J. Climate*, **31**, 9055–9071, https://doi.org/10.1175/JCLI-D-18-0515.1.

Tao, S. Y., and Y. H. Ding, 1981: Observational evidence of the influence of the Qinghai–Xizang (Tibet) Plateau on the occurrence of heavy rain and severe convective storms in China. *Bull. Amer. Meteor. Soc.*, **62**, 23–30, https://doi.org/10.1175/1520-0477(1981)062<0023:OEOTIO>2.0.CO;2.

Wang, B., and H. Rui, 1990: Synoptic climatology of transient tropical intraseasonal convection anomalies: 1975–1985. *Meteor. Atmos. Phys.*, **44**, 43–61, https://doi.org/10.1007/BF01026810.

——, and X. S. Xie, 1997: A model for the boreal summer intraseasonal oscillation. *J. Atmos. Sci.*, **54**, 72–86, https://doi.org/10.1175/1520-0469(1997)054<0072:AMFTBS>2.0.CO;2.

Wang, H., F. Liu, B. Wang, and T. Li, 2017: Effect of intraseasonal oscillation on South China Sea summer monsoon onset. *Climate Dyn.*, **51**, 2543–2558, https://doi.org/10.1007/s00382-017-4027-9.

Wang, M., and A. Duan, 2015: Quasi-biweekly oscillation over the Tibetan Plateau and its link with the Asian summer monsoon. *J. Climate*, **28**, 4921–4940, https://doi.org/10.1175/JCLI-D-14-00658.1.

Webster, P., 1983: Mechanisms of monsoon low-frequency variability: Surface hydrological effects. *J. Atmos. Sci.*, **40**, 2110–2124, https://doi.org/10.1175/1520-0469(1983)040<2110:MOMLFV>2.0.CO;2.

Wu, G. X., and Y. S. Zhang, 1998: Tibetan Plateau forcing and the timing of the monsoon onset over South Asian and the South China Sea. *Mon. Wea. Rev.*, **126**, 913–927, https://doi.org/10.1175/1520-0493(1998)126<0913:TPFATT>2.0.CO;2.

——, and Coauthors, 1997: Sensible heat driven air–pump over the Tibetan Plateau and its impacts on the Asian summer monsoon. *Collection in the Memory of Zhao Jiuzhang*, J. Zhao and D. Z. Ye, Eds., Chinese Science Press, 116–126.

——, and Coauthors, 2007: The influence of the mechanical and thermal forcing of the Tibetan Plateau on the Asian climate. *J. Hydrometeor.*, **8**, 770–789, https://doi.org/10.1175/JHM609.1.

——, Y. M. Liu, B. He, Q. Bao, A. M. Duan, and F.-F. Jin, 2012a: Thermal controls on the Asian summer monsoon. *Sci. Rep.*, **2**, 404, https://doi.org/10.1038/srep00404.

——, ——, B. W. Dong, X. Liang, A. Duan, Q. Bao, and J. Yu, 2012b: Revisiting Asian monsoon formation and change associated with Tibetan Plateau forcing: I. Formation. *Climate Dyn.*, **39**, 1169–1181, https://doi.org/10.1007/s00382-012-1334-z.

——, and Coauthors, 2015: Tibetan Plateau climate dynamics: Recent research progress and outlook. *Natl. Sci. Rev.*, **2**, 100–116, https://doi.org/10.1093/nsr/nwu045.

——, H. F. Zhuo, Z. Q. Wang, and Y. M. Liu, 2016: Two types of summertime heating over the Asian large-scale orography and excitation of potential-vorticity forcing I. Over Tibetan Plateau. *Sci. China Earth Sci.*, **59**, 1996–2008, https://doi.org/10.1007/s11430-016-5328-2.

——, B. He, A. M. Duan, Y. M. Liu, and W. Yu, 2017: Formation and variation of the atmospheric heat source over the Tibetan Plateau and its climate effects. *Adv. Atmos. Sci.*, **34**, 1169–1184, https://doi.org/10.1007/s00376-017-7014-5.

Xie, X., and B. Wang, 1996: Low-frequency equatorial waves in vertically sheared zonal flow. Part II: Unstable waves. *J. Atmos. Sci.*, **53**, 3589–3605, https://doi.org/10.1175/1520-0469(1996)053<3589:LFEWIV>2.0.CO;2.

Yanai, M., C. Li, and Z. Song, 1992: Seasonal heating of the Tibetan Plateau and its effects of the evolution of the Asian summer monsoon. *J. Meteor. Soc. Japan*, **70**, 319–351, https://doi.org/10.2151/jmsj1965.70.1B_319.

Yang, J., B. Wang, and Q. Bao, 2010: Biweekly and 21–30-day variations of the subtropical summer monsoon rainfall over the lower reach of the Yangtze River Basin. *J. Climate*, **23**, 1146–1159, https://doi.org/10.1175/2009JCLI3005.1.

Yang, Y. M., B. Wang, and J. Y. Lee, 2019: Mechanisms of northward propagation of boreal summer intraseasonal oscillation revealed by climate model experiments. *Geophys. Res. Lett.*, **46**, 3417–3425, https://doi.org/10.1029/2018GL081612.

Yasunari, T., 1979: Cloudiness fluctuations associated with the Northern Hemisphere summer monsoon. *J. Meteor. Soc. Japan*, **57**, 227–242, https://doi.org/10.2151/jmsj1965.57.3_227.

——, 1980: A quasi-stationary appearance of 30- to 40-day period in the cloudiness fluctuations during the summer monsoon over India. *J. Meteor. Soc. Japan*, **58**, 225–229, https://doi.org/10.2151/jmsj1965.58.3_225.

——, K. Saito, and K. Takata, 2006: Relative roles of large-scale orography and land surface processes in the global hydroclimate. Part I: Impacts on monsoon systems and the tropics. *J. Hydrometeor.*, **7**, 626–641, https://doi.org/10.1175/JHM515.1.

Ye, D. Z., and G. X. Wu, 1998: The role of the heat source of the Tibetan Plateau in the general circulation. *Meteor. Atmos. Phys.*, **67**, 181–198, https://doi.org/10.1007/BF01277509.

Yeh, T. C., 1950: The circulation of the high troposphere over China in the winter of 1945–1946. *Tellus*, **2**, 173–183, https://doi.org/10.3402/tellusa.v2i3.8548.

——, S. W. Luo, and P. C. Chu, 1957: The wind structure and heat balance in the lower troposphere over Tibetan Plateau and its surrounding. *Acta Meteor. Sin.*, **28**, 108–121, https://doi.org/10.11676/qxxb1957.010.

Zhao, P., and L. X. Chen, 2001: Climate features of atmospheric heat source/sink over the Qinghai-Xizang Plateau in 35 years and its relation to rainfall in China. *Sci. China Earth Sci.*, **44**, 858–864, https://doi.org/10.1007/BF02907098.

Zhong, S., J. Qiao, Z. Zhu, and X. Zhang, 2020: Two propagation pathways of the boreal summer quasi-biweekly oscillation of atmospheric heat source over the Tibetan Plateau. *Atmos.–Ocean*, **58**, 60–78, https://doi.org/10.1080/07055900.2020.1730297.

Zhu, Z., and T. Li, 2017: Empirical prediction of the onset dates of South China Sea summer monsoon. *Climate Dyn.*, **48**, 1633–1645, https://doi.org/10.1007/s00382-016-3164-x.

——, and ——, 2018: Extended-range forecasting of Chinese summer surface air temperature and heat waves. *Climate Dyn.*, **50**, 2007–2021, https://doi.org/10.1007/s00382-017-3733-7.